

Interface waves along fractures in anisotropic media

Siyi Shao¹ and Laura J. Pyrak-Nolte²

ABSTRACT

The detection of fractures in an anisotropic medium is complicated by discrete modes that are guided or confined by fractures such as fracture interface waves. Fracture interface waves are generalized coupled Rayleigh waves whose existence and velocity in isotropic media depend on the stiffness of the fracture, frequency of the source, and shear-wave polarization. We derived the analytic solution for fracture interface waves in an orthorhombic medium and found that the existence and velocity of interface waves in anisotropic media are also affected by the orientation of a fracture relative to the layering. Laboratory measurements of fracture interface waves using ultrasonic transducers (central frequency ~ 1 MHz) on garolite

specimens confirmed that the presence of fracture interface waves can mask the textural shear-wave anisotropy of waves propagating parallel to the layering. At low stresses, a layered medium appears almost isotropic when a fracture is oriented perpendicular to the layering, and conversely, a layered medium exhibits stronger anisotropy than the matrix for a fracture oriented parallel to the layering. The matrix shear-wave anisotropy is recovered when sufficient stress is applied to close a fracture. The theory and experimental results demonstrated that the interpretation of the presence of fractures in anisotropic material can be unambiguously interpreted if measurements are made as a function of stress, which eliminates many fractured-generated discrete modes such as fracture interface waves.

INTRODUCTION

Discontinuities such as fractures, joints, and faults occur in the earth's crust in a variety of rock types. Previous research has shown the existence of discrete modes caused by single and parallel sets of fractures. For example, several studies (Murty, 1975; Pyrak-Nolte and Cook, 1987; Suarez-Rivera, 1992; Gu et al., 1996; Pyrak-Nolte et al., 1996) have shown that fractures support coupled Rayleigh waves (also known as “fracture interface waves”) that propagate along fractures in an otherwise isotropic material. The existence of fracture interface waves depends on the wavelength of the signal, the fracture specific stiffness relative to the material properties of the matrix, and the polarization of a shear-wave source relative to the fracture plane. Nihei et al. (1994) showed theoretically the existence of Love waves in an isotropic medium, where the Love waves are guided by the presence of parallel fractures. Xian et al. (2001) demonstrated experimentally that leaky compressional-wave guided modes, occurring in sets of parallel fractures in an isotropic

medium, are sensitive to the stiffness distributions within the fracture sets and can propagate over at least 60 wavelengths.

Few studies have examined seismic-wave propagation in fractured anisotropic rocks (e.g., Kundu and Boström, 1992; Carcione, 1996, 1997, 1998; Rüger, 1998; Chaisri and Krebs, 2000; Carcione and Picotti, 2012). Schoenberg (2009) derived a second-rank compliance tensor (inverse of stiffness tensor) for a vertically fractured transversely isotropic medium with a set of parallel fractures to theoretically decompose the contribution into the fractures versus that from the matrix. However, effective medium approaches ignore the existence of fracture interface waves and other fracture guided modes that can affect seismic interpretations. Because these guided modes are frequency dependent, broadband data can result in the observation of both effective medium and discrete mode behavior, resulting in overlapping scattering regimes. For example, Nolte et al. (2000) demonstrated experimentally that different scattering regimes coexist when broadband sources are used. Specifically, they observed that the transition from long wavelength to short

Manuscript received by the Editor 2 November 2012; revised manuscript received 28 February 2013; published online 10 June 2013.

¹Purdue University, Department of Physics, West Lafayette, Indiana, USA. E-mail: shao5@purdue.edu.

²Purdue University, Department of Physics; Department of Earth and Atmospheric Sciences; School of Civil Engineering, West Lafayette, Indiana, USA. E-mail: ljpn@purdue.edu.

© 2013 Society of Exploration Geophysicists. All rights reserved.

wavelength scattering behavior for fracture interface waves is a smooth transition, where both interface waves and resonant-scattered Rayleigh waves are observed.

In this paper, we demonstrate the effect of fracture interface waves on the interpretation of seismic anisotropy of an orthorhombic medium for shear waves propagating parallel to the layering. We present the theoretical derivation for fracture interface waves in an orthorhombic medium for two specific conditions: (1) a fracture oriented perpendicular to the layering and (2) a fracture oriented parallel to the layering. In addition, we present the results from laboratory experiments that demonstrate and confirm the theoretical predictions that the presence of fracture interface waves can mask the matrix anisotropy. The theoretical and experimental results show that the background or matrix anisotropy is recovered as fractures close under normal stress.

THEORY

The existence and behavior of fracture-interface waves along fractures in isotropic material has been shown theoretically in previous works (e.g., Murty, 1975; Pyrak-Nolte and Cook, 1987; Gu et al., 1996). In those studies, a fracture is represented by a set of boundary conditions (often referred to as the “displacement discontinuity theory” or “linear-slip theory”). These nonwelded boundary conditions are that stress across a fracture is continuous, but the displacement is not. The discontinuity in displacement is inversely proportional to the specific stiffness of the fracture (Mindlin, 1960; Kendall and Tabor, 1971; Murty, 1975; Schoenberg, 1980; Kitsunozaki, 1983; Schoenberg, 1983; Myer et al., 1985; Pyrak-Nolte et al., 1990a, 1990b; Murty and Kumar, 1991; Suarez-Rivera, 1992; Gu, 1994).

Here, we present the theoretical derivation of fracture interface waves for a medium with a single fracture oriented either parallel

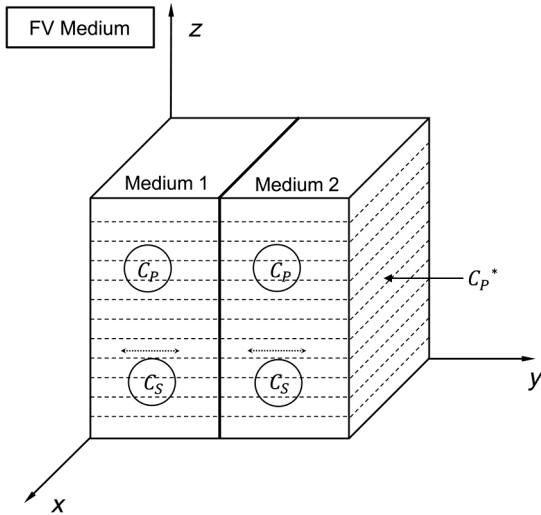


Figure 1. A sketch of a vertically fractured medium with a horizontal matrix layering (FV). A fracture lies in the x - z plane (the solid line), whereas all the layers lie in the x - y plane (dashed lines). Symbols C_P and C_P^* represent horizontal P-waves propagating along the x -axis and y -axis, respectively. Symbol C_S represents horizontally propagated S-waves, which are polarized parallel to layers as indicated by the dotted arrows in medium 1 and medium 2. All waves propagate in the intact portion of the media (not along or through the fracture).

(the FH medium), or perpendicular (the FV medium) to the matrix layering. In both cases, the layers of the matrix lie in the x - y plane. The layered matrix is considered as an orthorhombic or a modified vertically transversely isotropic (VTI) medium, and a fracture is represented as a nonwelded contact between two identical media (i.e., the same material density, and elastic constants).

Fracture perpendicular to layering (FV)

In the FV medium, a fracture is assumed to lie vertically in the x - z plane (solid line in Figure 1). The half space for $y > 0$ is medium 1, whereas the half space for $y < 0$ is medium 2. The displacement discontinuity boundary conditions that represent the fracture are

$$\begin{aligned} u_y^{(1)} - u_y^{(2)} &= \sigma_{yy}^{(1)} / \kappa_y, \\ \sigma_{yy}^{(1)} &= \sigma_{yy}^{(2)}, \\ u_x^{(1)} - u_x^{(2)} &= \sigma_{xy}^{(1)} / \kappa_x, \\ \sigma_{xy}^{(1)} &= \sigma_{xy}^{(2)}, \\ u_z^{(1)} - u_z^{(2)} &= \sigma_{yz}^{(1)} / \kappa_z, \\ \sigma_{yz}^{(1)} &= \sigma_{yz}^{(2)}, \end{aligned} \quad (1)$$

where κ_x and κ_z represent the shear-specific stiffnesses of the fracture, κ_y is the normal specific stiffness, and σ is a second-rank tensor representing stress across the fracture. Superscripts (1) and (2) indicate the parameters in medium 1 and medium 2, respectively.

A detailed derivation of the solution for fracture interface waves is given in Appendix A. Here, we present the secular equations for the symmetric interface wave,

$$\begin{aligned} &\left[\left(\frac{\eta_2^2 - \eta_3^2}{\eta_1^2} \right) (2\xi^4 - \xi^2 - 2\xi^2 \sqrt{\xi^2 - \eta_1^2} \sqrt{\xi^2 - 1}) - \eta_2^2 (2\xi^2 - 1) \right] \\ &- 2\sqrt{\xi^2 - \eta_1^2} \bar{\kappa}_y = 0, \end{aligned} \quad (2)$$

and, for the antisymmetric interface wave,

$$\begin{aligned} &\frac{1}{\eta_2^2} \left[\left(\frac{\eta_2^2 - \eta_3^2}{\eta_1^2} \right) (2\xi^4 - \xi^2 - 2\xi^2 \sqrt{\xi^2 - \eta_1^2} \sqrt{\xi^2 - 1}) - \eta_2^2 (2\xi^2 - 1) \right] \\ &- 2\sqrt{\xi^2 - 1} \bar{\kappa}_x = 0, \end{aligned} \quad (3)$$

where

$$\begin{aligned} \xi &= C_S / C, \\ \eta_1 &= C_S / C_P, \\ \eta_2 &= C_P^* / C_P, \\ \eta_3 &= \zeta / C_P. \end{aligned} \quad (4)$$

In equation 4, C is the fracture interface wave velocity, C_S is the S-wave velocity and C_P , C_P^* are P-wave velocities (Figure 1). The normalized normal stiffness is $\bar{\kappa}_y = \kappa_y / \omega Z_S$, and $\bar{\kappa}_x = \kappa_x / \omega Z_S$ is the normalized shear stiffness ($Z_S = \rho C_S$ is the shear-wave impedance, where ρ is medium density). Symbol ζ is a notation for convenience, and it can be expressed by the off diagonal stiffness component c_{12} (see Appendix A) and density ρ as

$$\zeta = \sqrt{c_{12}/\rho}. \quad (5)$$

The secular equations (equations 2 and 3) for the two interface modes are used to determine the range of existence and velocity of fracture interface waves. From equation 2, the symmetric mode existence depends only on the normal fracture specific stiffness κ_y whereas the existence of the antisymmetric mode depends only on the shear fracture specific stiffness κ_x (equation 3). Both modes also depend on the frequency of the signal. If the last term in equation 2 (or equation 3) is set to zero (i.e., fracture specific stiffness $\bar{\kappa}_y = \bar{\kappa}_x = 0$, and the surfaces are decoupled), the solution reverts to that for a Rayleigh wave.

C_S , C_P , and C_P^* were directly measured in our experiments (see “Experimental Approach” section). However, measuring ζ is more

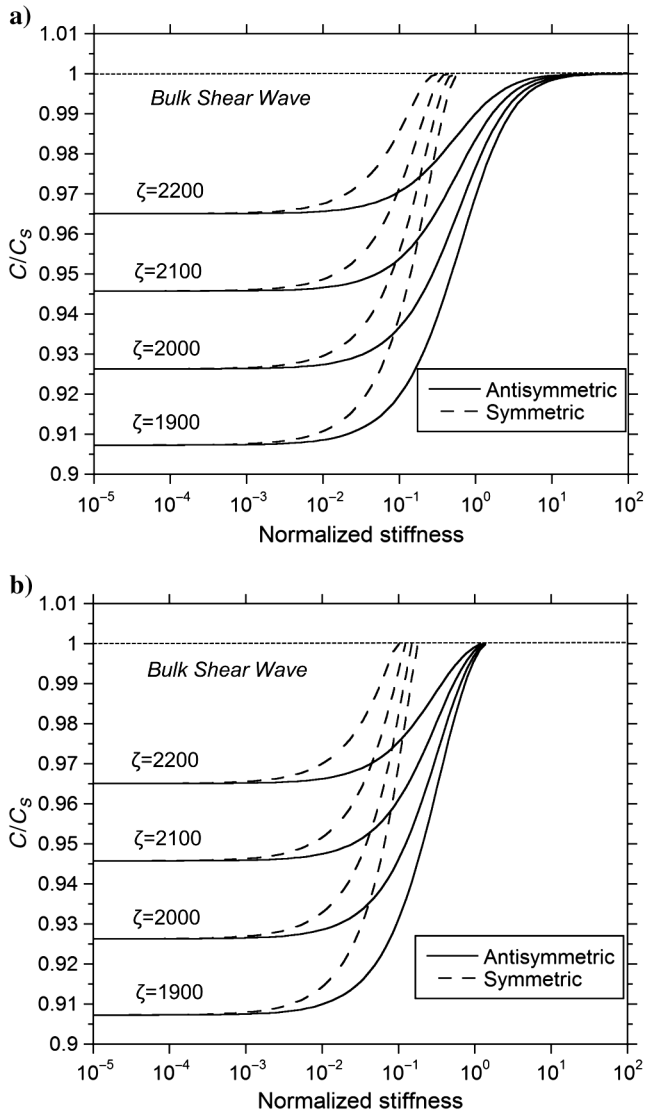


Figure 2. (a) Normalized interface-wave phase velocities (C/C_S) as a function of normalized stiffness in the FV medium for different ζ values. (b) Normalized interface-wave group velocities as a function of normalized stiffness in the FV medium for different ζ values. Here, in normalized stiffness $k/\omega Z$, C_S represents an S-wave polarized parallel to the layers.

complicated. In a VTI or orthorhombic medium, the off diagonal stiffness components c_{12} and c_{13} determine the azimuthally varying wave velocities. In this study, ζ is obtained by comparing the “simulated” Rayleigh wave velocities with the experimentally measured Rayleigh wave velocity. From a parameter study of the effect of ζ (i.e., c_{12}) on the interface wave velocities, it is observed that the value of ζ affects the Rayleigh wave velocity (Figure 2). The Rayleigh wave velocity increases with increasing ζ . We determined the value of ζ by comparing the theoretically derived Rayleigh wave velocities with the Rayleigh wave velocity from laboratory measurements.

Using the parameters from experimental measurements (Table 1), fracture interface wave velocities were obtained by numerically solving equations 2 and 3. Figure 3 shows the interface wave velocities (phase and group) normalized by the bulk shear-wave velocity (polarized parallel to the layers) as a function of normalized fracture specific stiffness $\bar{\kappa}_y$ (or $\bar{\kappa}_x$) as in the theoretical section. Like the isotropic case, the phase and group velocities range from the Rayleigh velocity at low fracture specific stiffness (or high frequency) when the fracture behaves like a free surface, to the bulk shear-wave velocity at higher fracture specific stiffness (or low frequency) when the fracture is essentially closed and behaves like a welded contact.

Fracture parallel to layering (FH)

Similar to the FV medium, equations for symmetric and antisymmetric interface waves were also derived for the case when the fracture and the layers are parallel to each other (the FH medium, see Figure 4). A detailed derivation for fracture interface waves for the FH medium is given in Appendix B.

The secular equation for symmetric interface waves in the FH medium is

$$\left(\frac{\eta_2^2 - \eta_4^2}{2\eta_1^2}\right) \left[(2\xi^2 - 1) \left(2\xi^2 - \frac{2\eta_1^2\eta_2^2}{\eta_2^2 - \eta_4^2} \right) - 4\xi^2 \sqrt{\xi^2 - 1} \sqrt{\xi^2 - \eta_1^2} \right] - 2\sqrt{\xi^2 - \eta_1^2} \cdot \bar{\kappa}_z = 0, \quad (6)$$

and for the antisymmetric interface wave is

$$\frac{(\eta_2^2 - \eta_4^2)\eta_3^2}{2\eta_1^4\eta_2^2} \left[(2\xi^2 - 1) \left(2\xi^2 - \frac{2\eta_1^2\eta_2^2}{\eta_2^2 - \eta_4^2} \right) - 4\xi^2 \sqrt{\xi^2 - 1} \sqrt{\xi^2 - \eta_1^2} \right] - 2\sqrt{\xi^2 - 1} \cdot \bar{\kappa}_x = 0, \quad (7)$$

Table 1. Parameter values used in solving equations 2 and 3. Values of the parameters (density, frequency, and wave velocities) are based on experimental measurements.

Parameters in mediums 1 and 2	Value
f (Frequency: MHz)	0.21
C_P (P-wave velocity: m/s)	3106
C_P^* (P-wave velocity: m/s)	2818
C_S (S-wave velocity: m/s)	1515
ζ (m/s)	2014
ρ (Density: kg/m ³)	1365

where

$$\begin{aligned}\xi &= C_S/C, \\ \eta_1 &= C_S/C_P, \\ \eta_2 &= C_P^*/C_P, \\ \eta_3 &= C_S^*/C_P, \\ \eta_4 &= \zeta/C_P.\end{aligned}\quad (8)$$

In equation 8, C_S , C_P , C_S^* , and C_P^* are S-wave and P-wave velocities, respectively (Figure 4). Similar to the FV medium, ζ is expressed in terms of the stiffness component c_{13} (see Appendix B), and density ρ as

$$\zeta = \sqrt{c_{13}/\rho}.\quad (9)$$

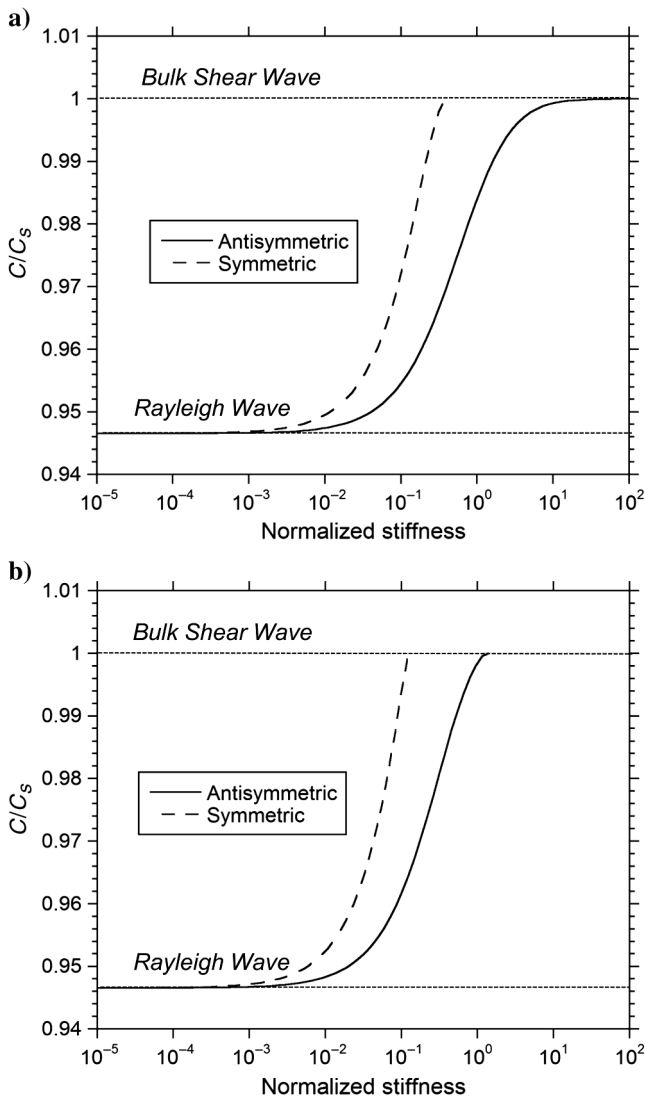


Figure 3. (a) Normalized fracture interface-wave phase velocities (symmetric and antisymmetric) as a function of normalized stiffness for the FV medium; (b) normalized fracture interface-wave group velocities as a function of normalized stiffness.

Here, C_S , C_P , C_S^* , and C_P^* were obtained from experimental measurements of S-waves and P-waves propagating either parallel or perpendicular to the layers (Figure 4), whereas ζ was obtained by fitting the Rayleigh-wave velocity. Figure 5 shows the effect of different values of ζ on the group and phase velocities of the slow and fast interface waves for an FH medium. As the values of c_{13} increases, the Rayleigh-wave velocity increases.

The velocities of both interface wave modes were examined for the conditions of our experiments. Table 2 lists all of the parameters obtained from experiments (described in section “Experimental Approach”) used to solve equations 6 and 7. Solutions corresponding to the symmetric and antisymmetric waves were found for the FH medium. Normalized phase and group velocities as a function of normalized stiffness are shown in Figure 6. The phase and group velocities exhibited similar trends as for the FV medium (Figure 3): phase and group velocities range from Rayleigh velocity at low stiffness, to bulk shear-wave velocities at higher stiffness. The main difference between the curves in Figures 3 and 6 is the value of the interface wave velocity at low stiffness (i.e., the Rayleigh-wave velocity), and the cut-off stiffness for the symmetric mode. The cut-off stiffness is the value of fracture specific stiffness for which the purely real symmetric mode no longer exists. Both these differences are attributed to the matrix anisotropy. For example, the low-velocity limit depends on the Rayleigh wave velocity, which in turns depends on the material properties of the matrix, i.e., the velocity of the Rayleigh wave differs for waves when propagating along a surface that is parallel to the layering versus a surface that is perpendicular to the layering.

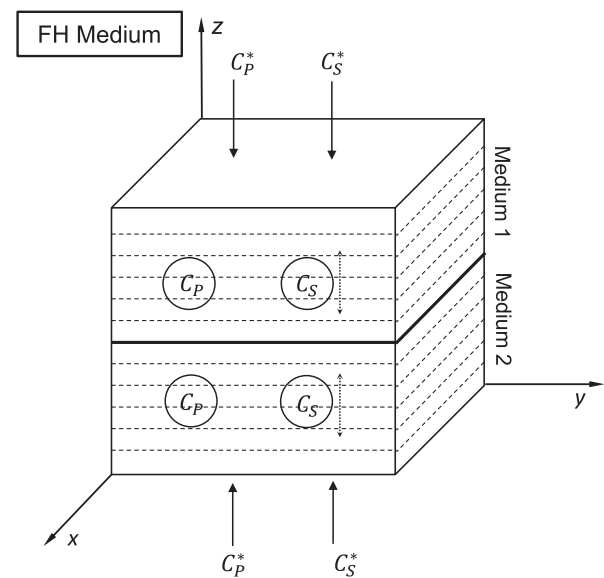


Figure 4. A sketch of a horizontally fractured medium with a horizontal matrix layering (FH). A fracture (the solid line) lies in the x - y plane as well as the layers (dashed lines). Symbols C_P and C_P^* represent horizontally and vertically propagated P-waves along the x -axis and z -axis, respectively. Symbols C_S and C_S^* represent horizontally and vertically propagated S-waves along the x -axis and z -axis, whereas the former one is polarized vertically (perpendicular to the layers). All waves propagate in the intact portion of the media (not along or through the fracture).

Shear-wave anisotropy in the FV and FH media

The existence of fracture interface waves can affect the interpretation of shear-wave anisotropy of an orthorhombic medium. Using the theoretically derived interface-wave velocities for the FV and FH media, we examined the “apparent” shear-wave anisotropy. Thomsen (1986) introduced the following equation to evaluate shear-wave anisotropy by elastic components as

$$\gamma = \frac{c_{66} - c_{44}}{2c_{44}}, \quad (10)$$

where in the FV and FH media, c_{66} depends on shear waves that are polarized parallel to the layers (which we refer to as an SH-wave with a velocity of V_{SH} in the x - z plane), and c_{44} depends on shear waves that are polarized perpendicular to the layers (referred to as an SV-wave with a velocity of V_{SV}).

Table 2. Parameter values used in solving equations 6 and 7. Values of the parameters (density, frequency, and wave velocities) are based on experimental measurements.

Parameters in mediums 1 and 2	Value
f (Frequency: MHz)	0.21
C_P (Horizontal P-wave velocity: m/s)	2966
C_S (Horizontal S-wave velocity: m/s)	1423
C_P^* (Vertical P-wave velocity: m/s)	2271
C_S^* (Vertical S-wave velocity: m/s)	1402
ζ (m/s)	1655
ρ (Density: kg/m ³)	1365

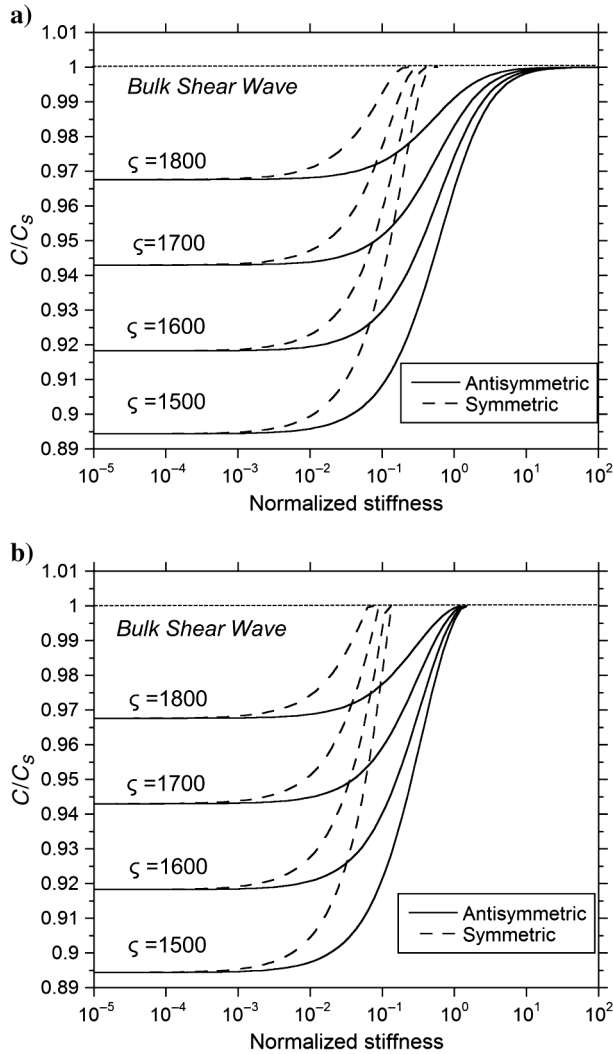


Figure 5. (a) Normalized interface-wave phase velocities (C/C_S) as a function of normalized stiffness in the FH medium for different ζ values. (b) Normalized interface-wave group velocities as a function of normalized stiffness in the FH medium for different ζ values. Here, in normalized stiffness $k/\omega Z$, C_S represents an S-wave polarized parallel to the layers.

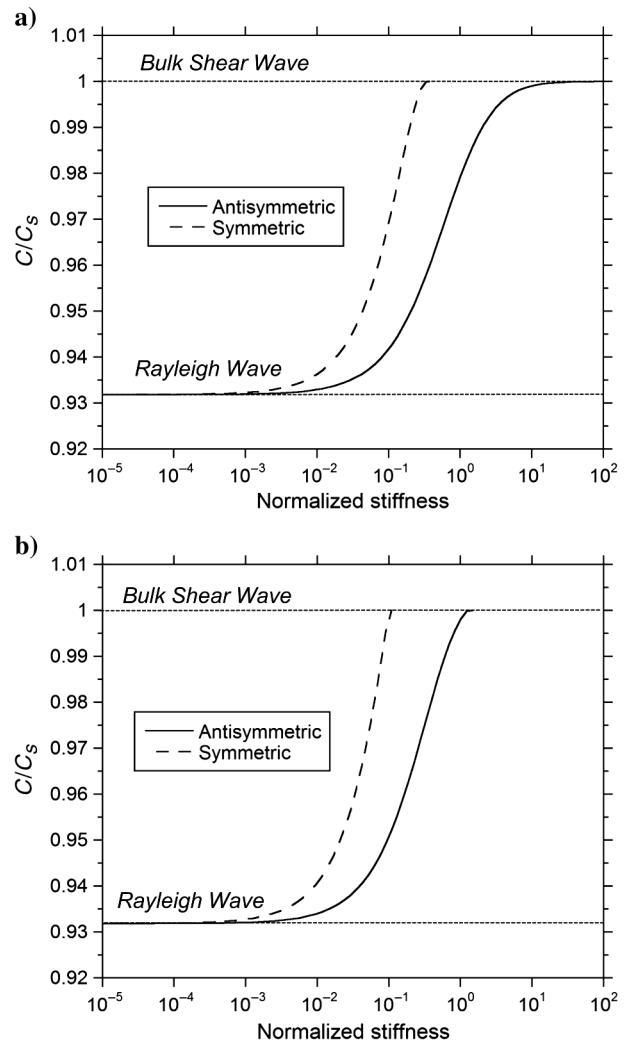


Figure 6. (a) Normalized fracture interface-wave phase velocities (symmetric and antisymmetric) as a function of normalized stiffness for the FH medium; (b) normalized fracture interface-wave group velocities as a function of normalized stiffness.

$$c_{66} = \rho V_{SH}^2, \quad c_{44} = \rho V_{SV}^2, \quad (11)$$

where γ can also be rewritten as

$$\gamma = \frac{1}{2} \left[\left(\frac{V_{SH}}{V_{SV}} \right)^2 - 1 \right]. \quad (12)$$

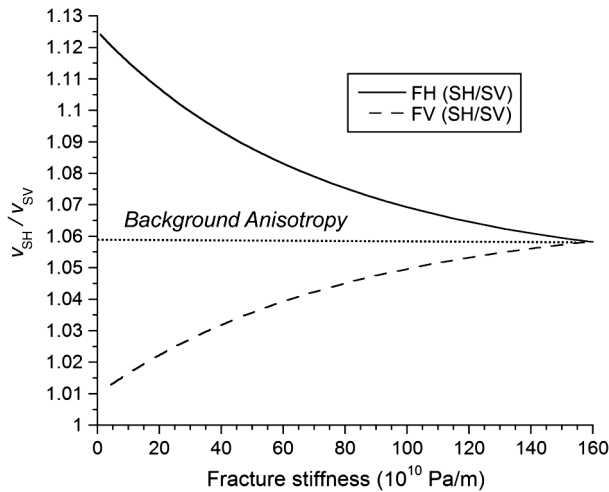


Figure 7. Theoretical ratio of group velocities, V_{SH}/V_{SV} , as a function of fracture-specific stiffness for two fractured media, FV and FH. The polarizations of shear waves are taken relative to the layers. The ratio approaches 1.06 (the background anisotropy ratio) when fracture stiffness increases.

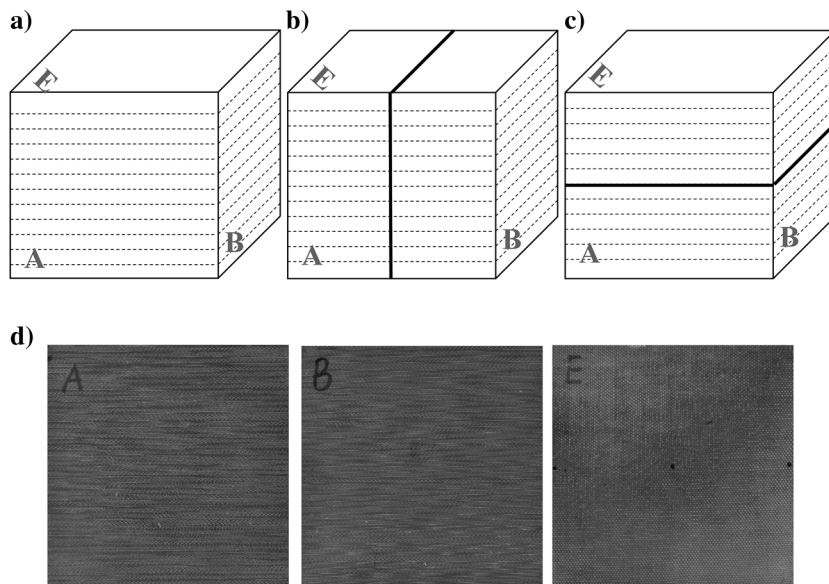


Figure 8. A sketch of the sample used in the experiments: (a) Intact containing no fractures, (b) FV with a fracture (solid line) perpendicular to the layers (dashed lines), (c) FH with a fracture parallel to the layers, (d) scans of three surfaces for the intact sample. The dashed thin lines indicate the layers, and the solid thick lines indicate the fracture in the samples. Capital letters A, B, etc., represent the face labels: face C is on the opposite side of face A, face D is on the opposite side of face B, and face F is on the opposite side of face E. The intact sample has layer planes parallel to face E. For the intact and the FH samples, the load is from E to F; for the FV sample, the load is from B to D.

Figure 7 shows the ratio of V_{SH} to V_{SV} (an indicator of shear-wave anisotropy exhibiting similar trends as γ) as a function of fracture-specific stiffness. When interface waves are present, the matrix anisotropy is masked at low values of fracture-specific stiffness. As stress on a fracture increased, fracture-specific stiffness increases because of the increase in contact area between the two surfaces and the reduction in the aperture. For the FH case, the ratio V_{SH}/V_{SV} increases from nearly isotropic ($V_{SH}/V_{SV} \sim 1$) to the background anisotropy ($V_{SH}/V_{SV} \sim 1.06$) with increasing stiffness. Conversely, when the fracture is perpendicular to the layers (the FV medium), the apparent anisotropy decreases from 1.12 to 1.06, i.e., to the ratio of V_{SH} to V_{SV} of the layered matrix. This demonstrates theoretically that the presence of fractures in a layered medium can lead to the misinterpretation of the shear-wave anisotropy when fracture interface waves are present, but not identified.

EXPERIMENTAL APPROACH

Seismic array experiments on intact and fractured orthorhombic samples

Experiments were performed on cubic samples ($\sim 100 \times 100 \times 100$ mm) of garolite, a high-performance fiber glass composite, to determine the effect of matrix anisotropy on the existence and velocity of interface waves, and the effect of fracture orientation on apparent shear-wave anisotropy. Garolite is a layered epoxy cloth laminate that is permanently assembled by heat, pressure, and adhesives. One intact and two fractured samples were used in this study and are shown in Figure 8. The synthetic fractures were fabricated by cutting the samples with a band saw and belt-sanding the surfaces. The difference between the two fractured samples FV and FH (see Figure 8b and 8c) is the orientation of the fracture relative to the layering in the matrix. The thickness of the layers in the matrix was on the order of 0.5 mm. A scan of three orthogonal surfaces of the intact sample are presented in Figure 8d for the layering planes that are parallel to face E, and that are observed on face A and B. In the FV sample, the fracture was oriented perpendicular to the layering, whereas in the FH sample, the fracture was oriented parallel to the layering (same definition as the FV medium and the FH medium in the “Theory” section). The dimensions of the samples are listed in Table 3 along with the densities of the samples that were determined gravimetrically. The uncertainty in the dimensions of the samples is approximately 50 micrometers. The Poisson’s ratios listed in Table 5 were based on the compressional (P-wave) and shear wave (S-wave) velocities measured on an intact sample or on intact portions of the fractured samples listed in Table 4. The intact sample was used as a reference to determine the seismic anisotropy of garolite for compressional and shear waves propagating in three orthogonal directions through the cubic samples. All of the samples were sealed with crystal clear tape to prevent the transducer couplant from penetrating into the samples during measurement.

relative to the layering in the matrix. The thickness of the layers in the matrix was on the order of 0.5 mm. A scan of three orthogonal surfaces of the intact sample are presented in Figure 8d for the layering planes that are parallel to face E, and that are observed on face A and B. In the FV sample, the fracture was oriented perpendicular to the layering, whereas in the FH sample, the fracture was oriented parallel to the layering (same definition as the FV medium and the FH medium in the “Theory” section). The dimensions of the samples are listed in Table 3 along with the densities of the samples that were determined gravimetrically. The uncertainty in the dimensions of the samples is approximately 50 micrometers. The Poisson’s ratios listed in Table 5 were based on the compressional (P-wave) and shear wave (S-wave) velocities measured on an intact sample or on intact portions of the fractured samples listed in Table 4. The intact sample was used as a reference to determine the seismic anisotropy of garolite for compressional and shear waves propagating in three orthogonal directions through the cubic samples. All of the samples were sealed with crystal clear tape to prevent the transducer couplant from penetrating into the samples during measurement.

A seismic array was used to send and receive P- and S-wave signals through the samples. The position of the array relative to the loading direction is shown in Figure 9 along with the layout of the P-wave and S-wave transducers. The load was always applied perpendicular to a fracture plane. The seismic array consisted of a source array and a receiver array each containing two P (Olympus-Panametrics V103) and five S (Olympus-Panametrics V153) contact piezoelectric transducers with a central frequency of 1 MHz. The transducer layouts for the source and receiver arrays were mirror images of each other. The S-wave transducers were polarized either perpendicular or parallel to the layers, as well as to the fracture. The transducers were coupled to a tape-sealed sample with honey that had been baked to reduce the water content 8.75% by weight. The couplant improves the coupling between the transducer and the machined, tape-covered surface of the sample. A pulse receiver (Panametrics 5077PR) was used to excite the source with a 0.4 microsecond duration square wave with a repetition rate of 100 Hz, amplitude of 400 V and a gain of +10 dB. The transducers and pulse receiver were coupled through a National Instrument PXI-1042 that used a PXI-5122 digitizer to record and store the full waveforms. For each transducer combination, a 100- μ s window

of the waveform, with a time delay of 4 μ s, was recorded with a resolution of 0.01 μ s/point.

The existence and velocity of interface waves depend on the specific stiffness of the fracture which increases with increasing stresses (see Bandis et al., 1983; Brown and Scholz, 1985, 1986; Hopkins et al., 1987, 1990; Pyrak-Nolte, 1996; Pyrak-Nolte and Morris, 2000). In this study, seismic measurements were performed as a function of stress to change the specific stiffness of the fractures. A uniaxial loading machine (Soiltest, Inc.) was used to apply loads normal to the fracture that ranged from 0 to 160 kN. The loads were applied in increments of either 8 or 80 kN. These applied loads resulted in normal stresses that ranged from 0 to 1.6 MPa.

Laser profilometer measurements

Laser profilometry was performed to measure the fracture surface roughness to determine if the asperity distribution differed for the two fractures because of the difference in their orientations relative to the layers. A semiconductor laser (KEYENCE LK-G152) with a wavelength of 650 nm was used to scan the fracture surface. Two linear stages (NEWPORT MTM250PP1) controlled by a motion controller (NEWPORT Universal Motion Controller ESP 300) moved the sample two dimensionally in a region of 100 \times 10 mm in a 0.1-mm increment.

Table 3. Material properties of the intact, FH, and FV samples.

Sample name	Intact	FH	FV
Dimension (mm)			
A to C	100.1	100.2	100.2
B to D	99.9	100.2	100.2
E to F	100.1	100.1	100.1
Density (kg/m ³)	1365	1360	1361

Table 4. P-wave and S-wave velocities (group) in the intact, FH, and FV samples. All data were taken from intact portions of the samples. When propagating along EF direction or perpendicular to layers, SH- and SV-waves are equivalent.

Sample name	Intact	FH	FV
SH-wave velocity (m/s)			
A to C	1507 \pm 0.2%	1510 \pm 0.6%	1515 \pm 0.2%
B to D	1513 \pm 0.4%	1501 \pm 0.2%	1519 \pm 0.3%
E to F	1410 \pm 0.6%	1402 \pm 0.2%	1418 \pm 0.1%
SV-wave velocity (m/s)			
A to C	1424 \pm 0.5%	1423 \pm 0.3%	1431 \pm 0.1%
B to D	1420 \pm 0.6%	1414 \pm 0.6%	1428 \pm 0.2%
E to F	1410 \pm 0.6%	1402 \pm 0.2%	1418 \pm 0.1%
P-wave velocity (m/s)			
A to C	3065 \pm 0.4%	2966 \pm 0.3%	3106 \pm 0.4%
B to D	2936 \pm 0.5%	3013 \pm 0.3%	2818 \pm 0.6%
E to F	2270 \pm 0.8%	2271 \pm 0.4%	2263 \pm 0.5%

Table 5. Poisson's ratio in the intact, FH, and FV samples.

Sample name	Intact	FH	FV
Poisson's ratio			
SH (A to C)	0.341 \pm 0.6%	0.325 \pm 1.0%	0.344 \pm 0.5%
SV (A to C)	0.362 \pm 0.6%	0.350 \pm 0.5%	0.365 \pm 0.6%
SH (B to D)	0.319 \pm 1.0%	0.335 \pm 0.5%	0.295 \pm 1.3%
SV (B to D)	0.347 \pm 0.9%	0.359 \pm 0.7%	0.327 \pm 0.9%
SH (E to F)	0.186 \pm 5.5%	0.192 \pm 2.3%	0.177 \pm 3.1%
SV (E to F)	0.186 \pm 5.5%	0.192 \pm 2.3%	0.177 \pm 3.1%

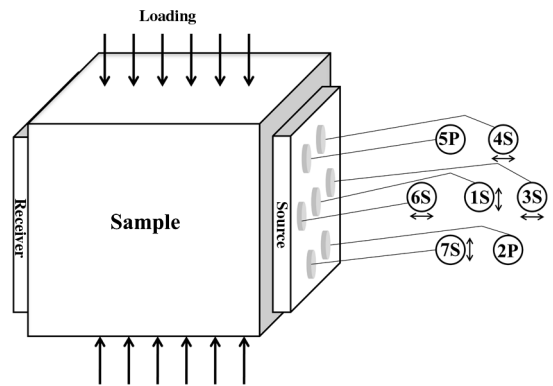


Figure 9. Sketch of a sample showing the location of the source and receiver arrays, the direction of loading and the distribution of P-wave and S-wave transducers. The S-wave polarization is indicated by the double-headed arrow below each S-wave transducer.

RESULTS

The seismic anisotropy for the garolite samples for waves propagating parallel to the layers was determined from measurements made on the intact sample. Shear waves transmitted through the intact sample are shown in Figure 10 for shear-wave transducers polarized parallel to the layering (SH) and perpendicular to the layering (SV). The shear waves are shown for normal stresses that ranged from 0 to 1.6 MPa and are relatively independent of stress (i.e., signals from all of the stresses overlap in Figure 10a). The difference in arrival time between the SV-wave and SH-wave is $4.022 \pm 0.066 \mu\text{s}$ and is insensitive to changes in stress. A wavelet transformation was performed on the signals to determine the group velocities for the SV- and SH-waves at a frequency of 0.21 MHz (see Pyrak-Nolte and Nolte, 1995; Nolte et al., 2000 for details of the wavelet transformation). Figure 10b shows the group velocity as

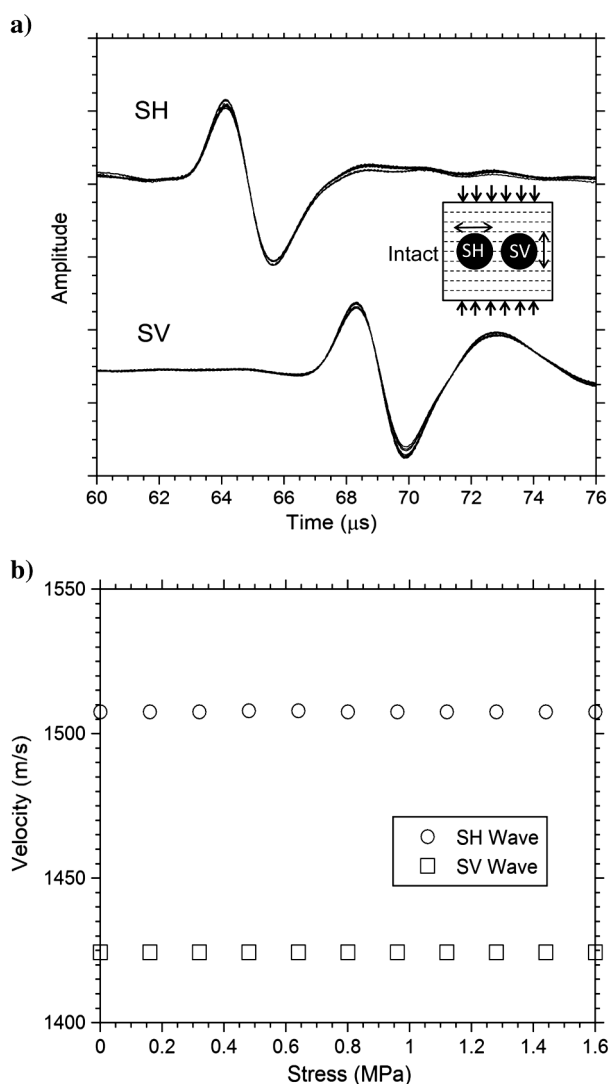


Figure 10. (a) Shear-wave signals from the intact sample for waves polarized parallel to the layering, SH, and perpendicular to the layering, SV. (b) Group velocity at 0.21 MHz of the waves shown in (a) as a function of stress. The small arrows indicate the load direction.

a function of stress for the SV- and SH-waves propagated through the intact sample. As expected for an orthorhombic medium, shear waves polarized perpendicular to the layers, have a lower group velocity (SV: $1424 \text{ m/s} \pm 0.1\%$) than that for shear waves polarized parallel to the layers (SH: $1507 \text{ m/s} \pm 0.2\%$). The ratio of group velocities, $V_{\text{SH}}/V_{\text{SV}}$, is approximately 1.06 and is independent of stress for the intact garolite.

When a fracture is oriented perpendicular to the layering (the FV sample), the SH-waves on the fracture no longer travel with the bulk shear-wave velocity, but travel instead as fracture-interface waves (Figure 11a). In this case, the SH-wave is stress-dependent whereas the SV-wave behavior is independent of stress. The observed stress dependent behavior of the SH-wave indicates that the energy is traveling as a fracture-interface wave. No interface wave is generated when shear waves are polarized parallel to a fracture. From the wavelet transformation, V_{SV} (perpendicular to the layers) is similar to the wave-velocity behavior of the intact sample (increased only from $1418 \text{ m/s} \pm 0.2\%$ to $1421 \text{ m/s} \pm 0.1\%$), while V_{SH} (parallel to the layers) increases with increasing stress ($1446 \text{ m/s} \pm 0.2\%$ to $1500 \text{ m/s} \pm 0.1\%$) (Figure 11b). The Rayleigh-wave velocity measured along the surface of the FV fracture (shear transducer polarized parallel to the layering), was around $1434 \text{ m/s} (\pm 0.5\%)$, which is smaller than the interface-wave velocity under no external load.

The converse is observed when the fracture is oriented parallel to the layering (the FH sample), i.e., the SV-waves on the fracture (perpendicular to layers) no longer travels with the bulk shear-wave velocity (Figure 12) and the behavior of the SH-waves (parallel to layers) were once more independent of stress; V_{SH} is constant ($1492 \text{ m/s} \pm 0.2\%$) with increasing stress, whereas V_{SV} increases from $1333 \text{ m/s} \pm 0.3\%$ to $1408 \text{ m/s} \pm 0.1\%$ for a stress increase of 1.6 MPa (Figure 12b). The SV-waves exhibit a decrease in arrival time with increasing stress and indicate that the SV-waves are traveling as fracture interface waves under lower stress. The Rayleigh wave measured along the surface of the FH fracture (shear transducer polarized perpendicular to the layering), exhibited a velocity of around $1324 \text{ m/s} (\pm 0.4\%)$, which is smaller than interface wave velocity under no external load.

DISCUSSION

As mentioned, fracture-interface waves are a form of generalized coupled Rayleigh waves that travel with a velocity that ranges between the Rayleigh-wave velocity and the bulk shear-wave velocity. The velocity of a fracture-interface wave is controlled by the properties of the matrix (density, seismic impedance) and the specific stiffness of the fracture. The ability to estimate fracture-specific or relative stiffness is important for predicting the hydraulic response of fractures. Previous research has shown that fracture-specific stiffness depends directly on the amount and distribution of contact area between the two fracture surfaces and is affected by the aperture distribution (Bandis et al., 1983; Pyrak-Nolte and Morris, 2000). Fluid flow through a fracture is implicitly linked to fracture-specific stiffness through the geometry of the fracture (Zimmerman, 1991; Cook, 1992; Pyrak-Nolte, 1996; Pyrak-Nolte and Morris, 2000; Petrovitch et al., 2013). Thus, seismic characterization of fracture-specific stiffness from interface waves has the potential to characterize relative fluid flow among fractures.

As mentioned, there are two types of nonvanishing interface waves: symmetric (fast wave) and antisymmetric (slow wave) waves (Pyrak-Nolte and Cook, 1987; Gu, 1994; Nihei et al., 1995).

In this study, we observed the antisymmetric or slow interface waves that only depend on the shear stiffness of the fracture. Our assumption that we are only observing the antisymmetric mode is based on the simulation work of Nihei et al. (1999) showing that the antisymmetric mode is best generated by a vertically polarized source (vertical to the fracture) such as that used in our experiments.

Applying the theory for fracture interface waves and the properties of the corresponding samples, two theoretical curves (for FV and FH, respectively, see Figure 13a) of normalized interface-wave velocity (the interface wave group velocity V_{IW} is normalized by the bulk shear-wave velocity V_S), are shown as a function of normalized stiffness, where the stiffness is normalized by seismic impedance, Z_S , (phase velocity \times density), and plane-wave angular frequency ω . The curves were generated for a frequency of 0.21 MHz, i.e., the frequency at which the group velocities were

determined for Figures 10, 11, and 12. The value of V_S and Z_S depend on the polarization of the shear-wave source relative to the layering.

Interface waves were observed for SH-waves in the FV sample and SV-waves in the FH sample, and exhibited group velocities in the range of the theoretical fracture interface waves (Figure 13a). From these results, the fracture specific stiffness was estimated and is shown as a function of stress in Figure 13b. For normal stresses less than 1 MPa, the estimated fracture stiffness of the fracture in the FV sample is slightly larger than that in the FH sample. At low stress, the difference in fracture specific stiffness for the two fractures is attributed to differences in the asperity height distributions (Figure 14). From the surface roughness measurement, the asperity heights in the FV fracture are more uniform than those in the FH fracture (Figure 14), i.e., a narrower distribution for FV. The

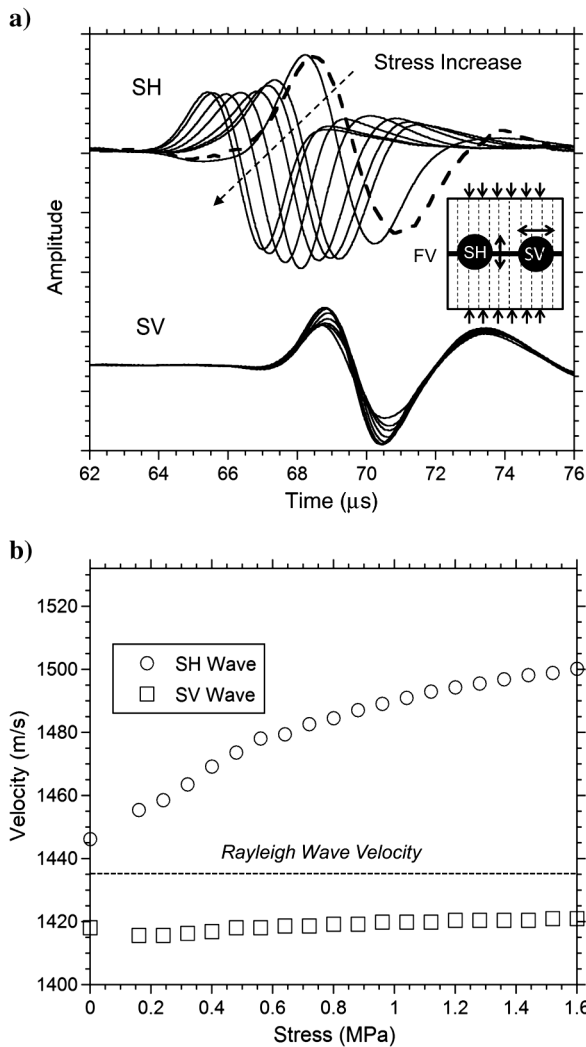


Figure 11. (a) Measured signals from the FV sample that contained a fracture perpendicular to the layering. The signals recorded for SH (polarization parallel to the layering) are fracture interface waves. (b) Group velocities at 0.21 MHz, V_{SH} and V_{SV} , as a function of stress for Sample FV. The dashed curve in (a) is the Rayleigh wave in this sample, whose velocity was indicated by the dashed line in (b). The small arrows indicate the load direction.

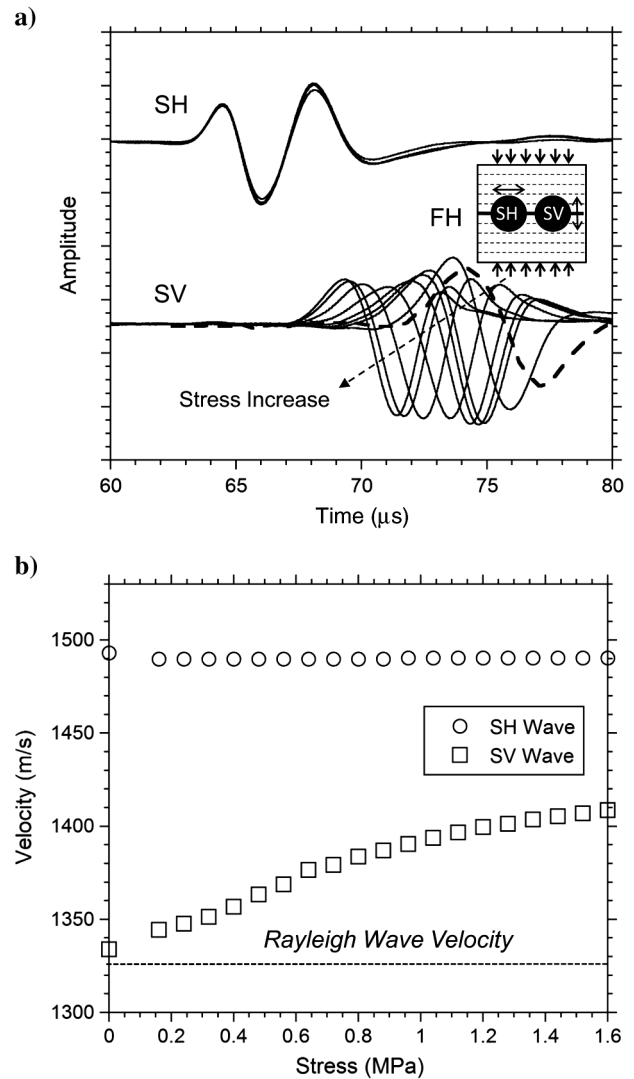


Figure 12. (a) Measured signals from the FH sample that contained a fracture parallel to the layering. The signals recorded for SV (polarization perpendicular to the layering) are fracture interface waves. (b) Group velocities at 0.21 MHz, V_{SH} and V_{SV} , as a function of stress for Sample FH. The dashed curve in (a) is the Rayleigh wave in this sample, whose velocity was indicated by the dashed line in (b). The small arrows indicate the load direction.

difference in asperity height occurs because the fracture in the FV sample cuts across the layering (i.e., cloth), whereas the fracture in the FH sample is parallel to the layering. The slightly faster increase in stiffness for the FH than the FV fracture indicates that the large apertures in the fracture are closing. For normal stresses higher than 1.2 MPa, the estimated fracture stiffness is close in value for FV and FH, which indicates a sufficient closing of the fractures. The interpreted fracture shear stiffness is consistent with the geometrical properties of the surfaces.

The interpretation of shear-wave splitting or apparent shear-wave anisotropy for a fractured layered medium depends on the orientation of a fracture relative to the layering in the sample. For the intact garolite sample, the ratio of the SH-wave group velocity to the SV-wave group velocity is approximately 1.06 and is independent of stress (for an intact sample or the intact portion of both the fractured samples), when waves were propagated parallel to the layering

(Figure 15). However, if a fracture is present and oriented perpendicular to the layering, the layered medium appears almost isotropic ($V_{SH}/V_{SV} \sim 1.02$) at low stress but recovers the matrix anisotropy ($V_{SH}/V_{SV} \sim 1.06$) at high stress (circles in Figure 15). Conversely, if a fracture is oriented parallel to the layering, the layered medium appears more anisotropic ($V_{SH}/V_{SV} \sim 1.12$) at low stress and also recovers the matrix anisotropy at high stress (squares in Figure 15). Theoretical calculations (Figure 7) of V_{SH}/V_{SV} as a function of fracture-specific stiffness exhibit very close values and trends consistent with the experimentally determined values. Thus, the existence of fracture interface waves can mask the matrix anisotropy of a medium if the fractures are not sufficiently closed and if these guided modes are not identified.

CONCLUSIONS

A question arises whether competing sources of anisotropy can be delineated for an anisotropic medium containing fractures. The

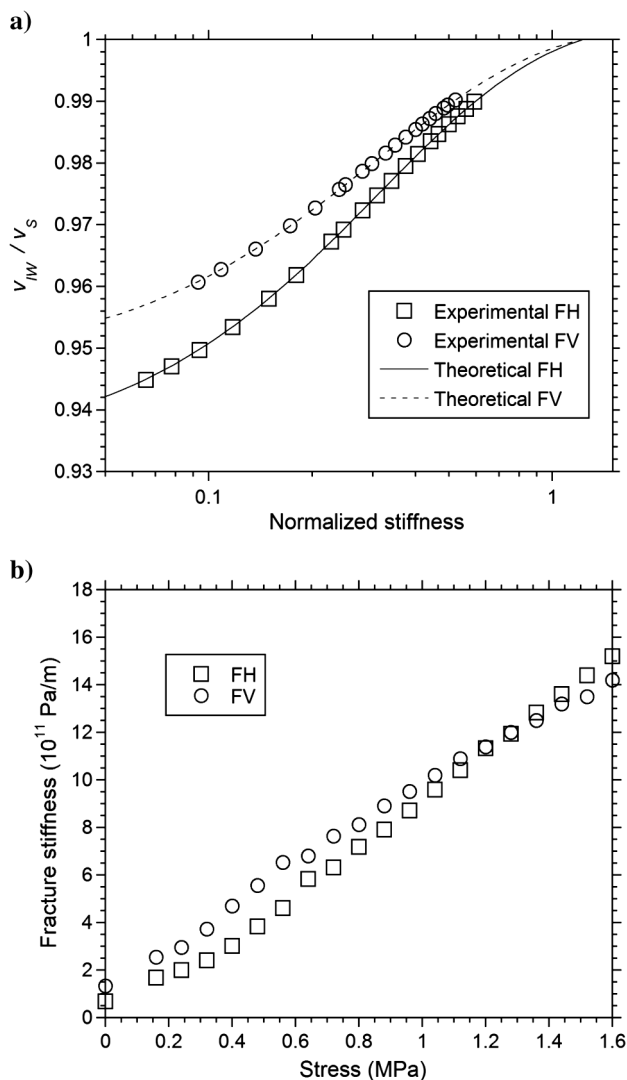


Figure 13. (a) Comparison of theoretical normalized group velocity as a function of normalized stiffness for fracture interface waves and measured values. (b) Estimated shear fracture-specific stiffness for the fractures in samples FV and FH.

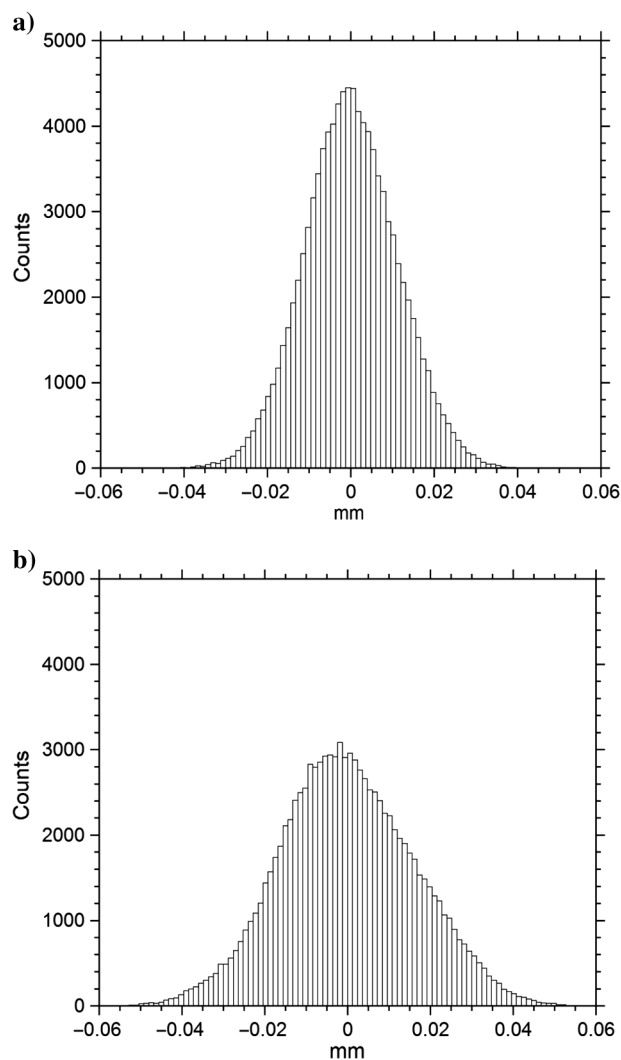


Figure 14. (a) Aperture distribution of the fracture surface of sample FV. (b) Aperture distribution of the fracture surface of sample FH. The x-axis indicates the derivation from the average height of each fracture surface.

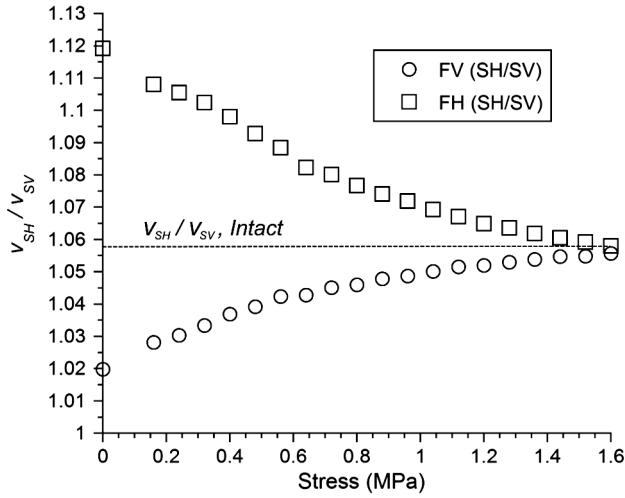


Figure 15. Experimental ratio of group velocities, V_{SH}/V_{SV} , as a function of stress for the intact sample, sample FV and FH. An isotropic sample would approach a ratio of 1.0.

results reported here demonstrate that the presence of just a single fracture can mask the matrix anisotropy caused by layering because of discrete guided-modes that occur along fractures. A medium can exhibit stronger or weaker anisotropy depending on the orientation of the fracture relative to the layering. More importantly, the matrix anisotropy can be recovered by increasing the fracture-specific stiffness through the application of stress, i.e., closing the fracture.

Because our experimental study was conducted at ultrasonic frequencies, it is necessary to address the question of the applicability of the theory to conditions in the field. The normalized stiffness used in the derivation of fracture interface waves is a scaling parameter that enables the application of this theory to other frequencies. The inverse of the normalized stiffness is normalized frequency given as $\omega Z_S/\kappa$. When $\omega Z_S/\kappa$ is between 1 and 100, fracture interface waves will exist and travel with speeds between the Rayleigh-wave and shear-wave velocity. For frequencies typically used in the field, only a bulk shear wave would be observed for fractures with specific stiffnesses commonly observed in laboratory samples ($\kappa \sim 10^{11} \rightarrow 10^{13}$ Pa/m). However, for a frequency of 10 Hz, fractures with specific stiffness that range between $10^6 \rightarrow 10^8$ Pa/m will support fracture-interface waves that travel with velocities between the Rayleigh- and shear-wave velocities.

Finally, future studies need to extend these concepts to multiple parallel fractures that, in addition to supporting fracture interface waves, will also support other modes that are guided between fractures. Ignoring the presence of guided modes in a fractured medium can result in mistaken interpretation of fracture orientation and matrix anisotropy.

ACKNOWLEDGMENTS

The authors wish to acknowledge support of this work by the Geosciences Research Program, Office of Basic Energy Sciences US Department of Energy (DE-FG02-09ER16022), and the Geomathematical Imaging group at Purdue University.

APPENDIX A

DERIVATION OF INTERFACE WAVES FOR MEDIUM FV

For the FV medium, the fracture is vertical in the x - z plane, and the symmetric axis of the layering is along the z -axis (Figure 1). Waves are propagated along the x -axis without z -components, but with exponentially decaying amplitudes along the y -direction. The geometry of this problem is simplified to the x - y plane, and the potentials for the fracture interface wave are expressed for the P-waves as

$$\begin{aligned}\phi^{(1)} &= A^{(1)} \exp[-p\omega y + i\omega(x/C - t)], \quad y \geq 0, \\ \phi^{(2)} &= A^{(2)} \exp[p\omega y + i\omega(x/C - t)], \quad y \leq 0, \quad (\text{A-1})\end{aligned}$$

and for the S-waves as

$$\begin{aligned}\psi^{(1)} &= B^{(1)} \exp[-q\omega y + i\omega(x/C - t)], \quad y \geq 0, \\ \psi^{(2)} &= B^{(2)} \exp[q\omega y + i\omega(x/C - t)], \quad y \leq 0, \quad (\text{A-2})\end{aligned}$$

where superscripts (1) and (2) refer to medium 1 and medium 2, ω is the angular frequency, t is the time, $A^{(1)}$, $A^{(2)}$, $B^{(1)}$ and $B^{(2)}$ are constants that need to be determined, C is the interface wave velocity, p and q are notations that can be expressed by P-wave velocity C_p and S-wave velocity C_s as

$$p = \sqrt{\frac{1}{C^2} - \frac{1}{C_p^2}}, \quad q = \sqrt{\frac{1}{C^2} - \frac{1}{C_s^2}}. \quad (\text{A-3})$$

The particle displacement is obtained by applying the following equations:

$$\begin{aligned}u_x^{(1)} &= \frac{\partial \phi^{(1)}}{\partial x} - \frac{\partial \psi^{(1)}}{\partial y}, & u_y^{(1)} &= \frac{\partial \phi^{(1)}}{\partial y} + \frac{\partial \psi^{(1)}}{\partial x}, \\ u_x^{(2)} &= \frac{\partial \phi^{(2)}}{\partial x} - \frac{\partial \psi^{(2)}}{\partial y}, & u_y^{(2)} &= \frac{\partial \phi^{(2)}}{\partial y} + \frac{\partial \psi^{(2)}}{\partial x}.\end{aligned} \quad (\text{A-4})$$

Hooke's law is used to relate stress ($\boldsymbol{\sigma}$) and strain ($\boldsymbol{\epsilon}$) via the elastic stiffness tensor \mathbf{C} ,

$$\boldsymbol{\sigma} = \mathbf{C}\boldsymbol{\epsilon}. \quad (\text{A-5})$$

For convenience in the following steps, we applied Voigt's notation ($xx \rightarrow 1, yy \rightarrow 2, zz \rightarrow 3, yz(z_y) \rightarrow 4, xz(z_x) \rightarrow 5, xy(y_x) \rightarrow 6$) to transform the stress and strain tensor ($\boldsymbol{\sigma}$ and $\boldsymbol{\epsilon}$) into vectors as

$$\begin{aligned}\boldsymbol{\sigma} &= (\sigma_{xx}, \sigma_{yy}, \sigma_{zz}, \sigma_{yz}, \sigma_{zx}, \sigma_{xy})^T = (\sigma_1, \sigma_2, \sigma_3, \sigma_4, \sigma_5, \sigma_6)^T, \\ \boldsymbol{\epsilon} &= (\epsilon_{xx}, \epsilon_{yy}, \epsilon_{zz}, \epsilon_{yz}, \epsilon_{zx}, \epsilon_{xy})^T = (\epsilon_1, \epsilon_2, \epsilon_3, \epsilon_4, \epsilon_5, \epsilon_6)^T,\end{aligned} \quad (\text{A-6})$$

and \mathbf{C} into a 6×6 second-rank tensor with eight independent components for the modified orthorhombic matrix (the shear modulus along the horizontal direction of the layers are assumed to be the same),

$$\begin{pmatrix} c_{11} & c_{12} & c_{13} & 0 & 0 & 0 \\ c_{12} & c_{22} & c_{23} & 0 & 0 & 0 \\ c_{13} & c_{23} & c_{33} & 0 & 0 & 0 \\ 0 & 0 & 0 & c_{44} & 0 & 0 \\ 0 & 0 & 0 & 0 & c_{44} & 0 \\ 0 & 0 & 0 & 0 & 0 & c_{66} \end{pmatrix}. \quad (\text{A-7})$$

We then express normal and shear stress for media 1 and 2 in terms of displacement as

$$\begin{aligned} \sigma_{yy}^{(1)} &= c_{12} \frac{\partial u_x^{(1)}}{\partial x} + c_{22} \frac{\partial u_y^{(1)}}{\partial y}, \\ \sigma_{xy}^{(1)} &= c_{66} \left(\frac{\partial u_x^{(1)}}{\partial y} + \frac{\partial u_y^{(1)}}{\partial x} \right), \\ \sigma_{yy}^{(2)} &= c_{12} \frac{\partial u_x^{(2)}}{\partial x} + c_{22} \frac{\partial u_y^{(2)}}{\partial y}, \\ \sigma_{xy}^{(2)} &= c_{66} \left(\frac{\partial u_x^{(2)}}{\partial y} + \frac{\partial u_y^{(2)}}{\partial x} \right), \end{aligned} \quad (\text{A-8})$$

where the diagonal components c_{11} , c_{22} , and c_{66} are expressed by wave velocities C_P , C_P^* , and C_S (Figure 1) with material density ρ as

$$c_{11} = \rho C_P^2, \quad c_{22} = \rho C_P^{*2}, \quad c_{66} = \rho C_S^2. \quad (\text{A-9})$$

We introduce ζ (with velocity dimension: [m/s]) to express the off diagonal component c_{12} ,

$$c_{12} = \rho \zeta^2. \quad (\text{A-10})$$

Applying the boundary conditions given in equation 1 in the main body of this paper, four linear equations are obtained:

$$\begin{aligned} \frac{i(\kappa_x + 2\omega\rho\rho C_S^2)}{C} A^{(1)} - \omega\rho C_S^2 \left(\frac{1}{C_S^2} - \frac{2}{C^2} \right) B^{(1)} + q\kappa_x B^{(1)} \\ - \frac{i\kappa_x}{C} A^{(2)} + q\kappa_x B^{(2)} = 0, \\ \omega\rho \left(\frac{C_P^{*2} - \zeta^2}{C^2} - \frac{C_P^{*2}}{C_P^2} \right) A^{(1)} + p\kappa_y A^{(1)} \\ + \frac{iq\omega\rho}{C} (\zeta^2 - C_P^{*2}) B^{(1)} - \frac{i\kappa_y}{C} B^{(1)} + p\kappa_y A^{(2)} + \frac{i\kappa_y}{C} B^{(2)} = 0, \\ \frac{2ip}{C} (A^{(1)} + A^{(2)}) + \left(\frac{2}{C^2} - \frac{1}{C_S^2} \right) (B^{(1)} - B^{(2)}) = 0, \\ \left(\frac{C_P^{*2} - \zeta^2}{C^2} - \frac{C_P^{*2}}{C_P^2} \right) (A^{(1)} - A^{(2)}) \\ + \frac{iq}{C} (C_P^{*2} - \zeta^2) (B^{(1)} + B^{(2)}) = 0. \end{aligned} \quad (\text{A-11})$$

When $A^{(1)} = A^{(2)}$, $B^{(1)} = -B^{(2)}$, the equation for the symmetric interface wave is derived,

$$\begin{aligned} \left[\left(\frac{\eta_2^2 - \eta_3^2}{\eta_1^2} \right) (2\xi^4 - \xi^2 - 2\xi^2 \sqrt{\xi^2 - \eta_1^2} \sqrt{\xi^2 - 1}) - \eta_2^2 (2\xi^2 - 1) \right] \\ - 2\sqrt{\xi^2 - \eta_1^2} \bar{\kappa}_y = 0, \end{aligned} \quad (\text{A-12})$$

and when $A^{(1)} = -A^{(2)}$, $B^{(1)} = B^{(2)}$, the equation for antisymmetric wave is (detailed explanation of symmetric and antisymmetric interface waves can be found in Pyrak-Nolte and Cook, 1987; Nihei et al., 1995; Gu et al., 1996)

$$\begin{aligned} \frac{1}{\eta_2^2} \left[\left(\frac{\eta_2^2 - \eta_3^2}{\eta_1^2} \right) (2\xi^4 - \xi^2 - 2\xi^2 \sqrt{\xi^2 - \eta_1^2} \sqrt{\xi^2 - 1}) - \eta_2^2 (2\xi^2 - 1) \right] \\ - 2\sqrt{\xi^2 - 1} \bar{\kappa}_x = 0, \end{aligned} \quad (\text{A-13})$$

where $\xi = C_S/C$, $\eta_1 = C_S/C_P$, $\eta_2 = C_P^*/C_P$, $\eta_3 = \zeta/C_P$, normalized normal stiffness $\bar{\kappa}_y = \kappa_y/\omega Z_S$, and shear stiffness $\bar{\kappa}_x = \kappa_x/\omega Z_S$ ($Z_S = \rho C_S$ is the shear-wave impedance).

APPENDIX B

DERIVATION OF INTERFACE WAVES FOR MEDIUM FH

For the FH medium, the fracture and layers lies in the x - y plane (Figure 4). The derivation procedure is similar to that for the FV medium (same forms for the wave potential, displacement, and boundary conditions). The stiffness tensor \mathbf{C} for a orthorhombic matrix has the same form as the FV medium (equation A-7).

The normal and shear stresses for media 1 and 2 in terms of displacement are

$$\begin{aligned} \sigma_{zz}^{(1)} &= c_{13} \frac{\partial u_x^{(1)}}{\partial x} + c_{33} \frac{\partial u_z^{(1)}}{\partial z}, \\ \sigma_{xz}^{(1)} &= c_{44} \left(\frac{\partial u_x^{(1)}}{\partial z} + \frac{\partial u_z^{(1)}}{\partial x} \right), \\ \sigma_{zz}^{(2)} &= c_{13} \frac{\partial u_x^{(2)}}{\partial x} + c_{33} \frac{\partial u_z^{(2)}}{\partial z}, \\ \sigma_{xz}^{(2)} &= c_{44} \left(\frac{\partial u_x^{(2)}}{\partial z} + \frac{\partial u_z^{(2)}}{\partial x} \right), \end{aligned} \quad (\text{B-1})$$

where c_{33} and c_{44} can be expressed by wave velocities C_S^* , C_P^* (propagated perpendicular through layers) and material density ρ as (see Figure 4)

$$c_{33} = \rho C_P^{*2}, \quad c_{44} = \rho C_S^{*2}. \quad (\text{B-2})$$

Notation ζ is also introduced to express the off diagonal component c_{13} ,

$$c_{13} = \rho \zeta^2. \quad (\text{B-3})$$

Using the boundary condition given in equation 1 in the main body, four linear equations are obtained:

$$\begin{aligned}
& \frac{i(\kappa_x + 2\omega\rho\rho C_S^{*2})}{C} A^{(1)} - \omega\rho C_S^{*2} \left(\frac{1}{C_S^2} - \frac{2}{C^2} \right) B^{(1)} + q\kappa_x B^{(1)} \\
& - \frac{i\kappa_x}{C} A^{(2)} + q\kappa_x B^{(2)} = 0, \\
& \frac{i(\kappa_z + 2\omega\rho\rho\zeta^2)}{C} B^{(1)} + \omega\rho \left(\frac{C_P^{*2}}{C_P^2} - \frac{2\zeta^2}{C^2} \right) A^{(1)} - p\kappa_z A^{(1)} \\
& - \frac{i\kappa_z}{C} B^{(2)} - p\kappa_z A^{(2)} = 0, \\
& \frac{2ip}{C} (A^{(1)} + A^{(2)}) + \left(\frac{1}{C^2} + q^2 \right) (B^{(1)} - B^{(2)}) = 0, \\
& \left(\frac{C_P^{*2}}{C_P^2} - \frac{2\zeta^2}{C^2} \right) (A^{(1)} - A^{(2)}) + \frac{2iq\zeta^2}{C} (B^{(1)} + B^{(2)}) = 0. \quad (\text{B-4})
\end{aligned}$$

When $A^{(1)} = A^{(2)}$, $B^{(1)} = -B^{(2)}$, the equation for a symmetric interface wavefield is obtained:

$$\begin{aligned}
& \left(\frac{\eta_2^2 - \eta_4^2}{2\eta_1^2} \right) \left[(2\xi^2 - 1) \left(2\xi^2 - \frac{2\eta_1^2\eta_2^2}{\eta_2^2 - \eta_4^2} \right) - 4\xi^2 \sqrt{\xi^2 - 1} \sqrt{\xi^2 - \eta_1^2} \right] \\
& - 2\sqrt{\xi^2 - \eta_1^2} \cdot \bar{\kappa}_z = 0. \quad (\text{B-5})
\end{aligned}$$

When $A^{(1)} = -A^{(2)}$, $B^{(1)} = B^{(2)}$, we get the equation for an anti-symmetric wavefield,

$$\begin{aligned}
& \frac{(\eta_2^2 - \eta_4^2)\eta_3^2}{2\eta_1^4\eta_2^2} \left[(2\xi^2 - 1) \left(2\xi^2 - \frac{2\eta_1^2\eta_2^2}{\eta_2^2 - \eta_4^2} \right) - 4\xi^2 \sqrt{\xi^2 - 1} \sqrt{\xi^2 - \eta_1^2} \right] \\
& - 2\sqrt{\xi^2 - 1} \cdot \bar{\kappa}_x = 0, \quad (\text{B-6})
\end{aligned}$$

where

$$\begin{aligned}
\xi &= C_S/C, \\
\eta_1 &= C_S/C_P, \\
\eta_2 &= C_P^*/C_P, \\
\eta_3 &= C_S^*/C_P, \\
\eta_4 &= \zeta/C_P. \quad (\text{B-7})
\end{aligned}$$

In this case, C is the interface wave velocity, $\bar{\kappa}_z = \kappa_z/\omega Z_S$ is the normalized normal stiffness, and the normalized shear stiffness is $\bar{\kappa}_x = \kappa_x/\omega Z_S$ ($Z_S = \rho C_S$ is the shear-wave impedance).

REFERENCES

- Bandis, S. C., A. C. Luden, and N. R. Barton, 1983, Fundamentals of rock joint deformation: *International Journal of Rock Mechanics and Mining Sciences & Geomechanics Abstracts*, **20**, 249–268, doi: [10.1016/0148-9062\(83\)90595-8](https://doi.org/10.1016/0148-9062(83)90595-8).
- Brown, S. R., and C. H. Scholz, 1985, Closure of random elastic surfaces in contact: *Journal of Geophysical Research, Solid Earth*, **90**, 5531–5545, doi: [10.1029/JB090iB07p05531](https://doi.org/10.1029/JB090iB07p05531).
- Brown, S. R., and C. H. Scholz, 1986, Closure of rock joints: *Journal of Geophysical Research, Solid Earth*, **91**, 4939–4948, doi: [10.1029/JB091iB05p04939](https://doi.org/10.1029/JB091iB05p04939).
- Carcione, J. M., 1996, Elastodynamics of a non-ideal interface: Application to crack and fracture scattering: *Journal of Geophysical Research, Solid Earth*, **101**, 28177–28188, doi: [10.1029/96JB02658](https://doi.org/10.1029/96JB02658).
- Carcione, J. M., 1997, Reflection and transmission of qP - qS plane waves at a plane boundary between viscoelastic transversely isotropic media: *Geophysical Journal International*, **129**, 669–680, doi: [10.1111/j.1365-246X.1997.tb04502.x](https://doi.org/10.1111/j.1365-246X.1997.tb04502.x).

- Carcione, J. M., 1998, Scattering of elastic waves by a plane crack of finite width in a transversely isotropic medium: *International Journal for Numerical and Analytical Methods in Geomechanics*, **22**, 263–275, doi: [10.1002/\(SICI\)1096-9853\(199804\)22:4<263::AID-NAG917>3.0.CO;2-S](https://doi.org/10.1002/(SICI)1096-9853(199804)22:4<263::AID-NAG917>3.0.CO;2-S).
- Carcione, J. M., and S. Picotti, 2012, Reflection and transmission coefficients of a fracture in transversely isotropic media: *Studia Geophysica et Geodaetica*, **56**, doi: [10.1007/s11200-011-9034-4](https://doi.org/10.1007/s11200-011-9034-4).
- Chaisri, S., and E. S. Krebs, 2000, Exact and approximate formulas for P - SV reflection and transmission coefficients for a nonwelded contact interface: *Journal of Geophysical Research, Solid Earth*, **105**, 28045–28054, doi: [10.1029/2000JB900296](https://doi.org/10.1029/2000JB900296).
- Cook, N. G. W., 1992, Natural joints in rock: Mechanical, hydraulic, and seismic behavior and properties under stress: *International Journal of Rock Mechanics and Mining Sciences & Geomechanics Abstracts*, **29**, 198–223, doi: [10.1016/0148-9062\(92\)93656-5](https://doi.org/10.1016/0148-9062(92)93656-5).
- Gu, B., 1994, Interface waves on a fracture in rock: Ph.D. thesis, University of California, Berkeley.
- Gu, B., K. T. Nihei, L. R. Myer, and L. J. Pyrak-Nolte, 1996, Fracture interface waves: *Journal of Geophysical Research, Solid Earth*, **101**, 827–835, doi: [10.1029/95JB02846](https://doi.org/10.1029/95JB02846).
- Hopkins, D. L., N. G. W. Cook, and L. R. Myer, 1987, Fracture stiffness and aperture as a function of applied stress and contact geometry: *Rock mechanics: Proceedings of the 28th US Symposium*, 673–680.
- Hopkins, D. L., N. G. W. Cook, and L. R. Myer, 1990, Normal joint stiffness as a function of spatial geometry and surface roughness: *Proceedings of the International Symposium on Rock Joints*, 203–210.
- Kendall, K., and D. Tabor, 1971, An ultrasonic study of the area of contact between stationary and sliding surfaces: *Proceedings of the Royal Society of London. Series A, Mathematical and Physical Science*, **323**, 321–340, doi: [10.1098/rspa.1971.0108](https://doi.org/10.1098/rspa.1971.0108).
- Kitsunezaki, C., 1983, Behavior of plane waves across a plane crack: *Journal of the Mining College, Akita University — Series A: Mining Geology*, **3**, 173–187.
- Kundu, T., and A. Boström, 1992, Elastic wave scattering by a circular crack in a transversely isotropic solid: *Wave Motion*, **15**, 285–300, doi: [10.1016/0165-2125\(92\)90012-Q](https://doi.org/10.1016/0165-2125(92)90012-Q).
- Mindlin, R. D., 1960, Waves and vibrations in isotropic planes: J. W. Goodier, and W. J. Hoff, Editors.
- Murty, G. S., 1975, A theoretical model for the attenuation and dispersion of Stoneley waves at the loosely bonded interface of elastic half-spaces: *Physics of the Earth and Planetary Interiors*, **11**, 65–79, doi: [10.1016/0031-9201\(75\)90076-X](https://doi.org/10.1016/0031-9201(75)90076-X).
- Murty, G. S., and V. Kumar, 1991, Elastic wave propagation with kinematic discontinuity along a non-ideal interface between two isotropic elastic half-spaces: *Journal of Nondestructive Evaluation*, **10**, 39–53, doi: [10.1007/BF00568099](https://doi.org/10.1007/BF00568099).
- Myer, L. R., D. L. Hopkins, and N. G. W. Cook, 1985, Effects of contact area of an interface on acoustic wave transmission characteristics: Presented at the US Rock Mechanics Symposium.
- Nihei, K. T., B. Gu, L. J. Pyrak-Nolte, and N. G. W. Cook, 1995, Elastic interface wave propagation along a fracture, in T. Fujii, ed., *Proceedings of the 8th International Congress on rock mechanics*, 1151–1157.
- Nihei, K. T., L. R. Myer, N. G. W. Cook, and W. D. Yi, 1994, Effects of non-welded interfaces on guided SH-waves: *Geophysical Research Letters*, **21**, 745–748, doi: [10.1029/94GL00365](https://doi.org/10.1029/94GL00365).
- Nihei, K. T., W. Yi, L. R. Myer, and N. G. W. Cook, 1999, Fracture channel waves: *Journal of Geophysical Research, Solid Earth*, **104**, 4769–4781, doi: [10.1029/1998JB900100](https://doi.org/10.1029/1998JB900100).
- Nolte, D. D., L. J. Pyrak-Nolte, J. Beachy, and C. Ziegler, 2000, Transition from the displacement discontinuity limit to the resonant scattering regime for fracture interface waves: *International Journal of Rock Mechanics and Mining Sciences & Geomechanics Abstracts*, **37**, 219–230, doi: [10.1016/S1365-1609\(99\)00102-1](https://doi.org/10.1016/S1365-1609(99)00102-1).
- Petrovitch, C. L., L. J. Pyrak-Nolte, and D. D. Nolte, 2013, Scaling of fluid flow versus fracture stiffness: *Geophysical Research Letters*, doi: [10.1002/grl.50479](https://doi.org/10.1002/grl.50479).
- Pyrak-Nolte, L. J., 1996, The seismic response of fractures and the interrelations among fracture properties: *International Journal of Rock Mechanics and Mining Sciences and Geomechanics Abstracts*, **33**, 787–802, doi: [10.1016/S0148-9062\(96\)00022-8](https://doi.org/10.1016/S0148-9062(96)00022-8).
- Pyrak-Nolte, L. J., and N. G. W. Cook, 1987, Elastic interface waves along a fracture: *Geophysical Research Letters*, **14**, 1107–1110, doi: [10.1029/GL014i011p01107](https://doi.org/10.1029/GL014i011p01107).
- Pyrak-Nolte, L. J., and J. P. Morris, 2000, Single fractures under normal stress: The relation between fracture specific stiffness and fluid flow: *International Journal of Rock Mechanics and Mining Sciences & Geomechanics Abstracts*, **37**, 245–262, doi: [10.1016/S1365-1609\(99\)00104-5](https://doi.org/10.1016/S1365-1609(99)00104-5).
- Pyrak-Nolte, L. J., L. R. Myer, and N. G. W. Cook, 1990a, Anisotropy in seismic velocities and amplitudes from multiple parallel fractures: *Journal of Geophysical Research, Solid Earth*, **95**, 11345–11358, doi: [10.1029/JB095iB07p11345](https://doi.org/10.1029/JB095iB07p11345).

- Pyrak-Nolte, L. J., L. R. Myer, and N. G. W. Cook, 1990b, Transmission of seismic-waves across single natural fractures: *Journal of Geophysical Research, Solid Earth*, **95**, 8617–8638, doi: [10.1029/JB095iB06p08617](https://doi.org/10.1029/JB095iB06p08617).
- Pyrak-Nolte, L. J., and D. D. Nolte, 1995, Wavelet analysis of velocity dispersion of elastic interface waves propagating along a fracture: *Geophysical Research Letters*, **22**, 1329–1332, doi: [10.1029/95GL01323](https://doi.org/10.1029/95GL01323).
- Pyrak-Nolte, L. J., S. Roy, and B. L. Mullenbach, 1996, Interface waves propagated along a fracture: *Journal of Applied Geophysics*, **35**, 79–87, doi: [10.1016/0926-9851\(96\)00009-2](https://doi.org/10.1016/0926-9851(96)00009-2).
- Rüger, A., 1998, Variation of P-wave reflectivity with offset and azimuth in anisotropic media: *Geophysics*, **63**, 935–947, doi: [10.1190/1.1444405](https://doi.org/10.1190/1.1444405).
- Schoenberg, M., 1980, Elastic wave behavior across linear slip interfaces: *Journal of the Acoustical Society of America*, **68**, 1516–1521, doi: [10.1121/1.385077](https://doi.org/10.1121/1.385077).
- Schoenberg, M., 1983, Reflection of elastic waves from periodically stratified media with interfacial slip: *Geophysical Prospecting*, **31**, 265–292, doi: [10.1111/j.1365-2478.1983.tb01054.x](https://doi.org/10.1111/j.1365-2478.1983.tb01054.x).
- Schoenberg, M., 2009, Vertically fractured transversely isotropic media: Dimensionality and deconstruction: *Geophysical Prospecting*, **57**, 169–185, doi: [10.1111/j.1365-2478.2008.00775.x](https://doi.org/10.1111/j.1365-2478.2008.00775.x).
- Suarez-Rivera, R., 1992, The influence of thin clay layers containing liquids on the propagation of shear waves: Ph.D. thesis, University of California, Berkeley.
- Thomsen, L., 1986, Weak elastic anisotropy: *Geophysics*, **51**, 1954–1966, doi: [10.1190/1.1442051](https://doi.org/10.1190/1.1442051).
- Xian, C., D. D. Nolte, and L. J. Pyrak-Nolte, 2001, Compressional waves guided between parallel fractures: *International Journal of Rock Mechanics and Mining Sciences & Geomechanics Abstracts*, **38**, 765–776, doi: [10.1016/S1365-1609\(01\)00041-7](https://doi.org/10.1016/S1365-1609(01)00041-7).
- Zimmerman, R. W., 1991, *Compressibility of sandstones*: Elsevier, **29**.